Research Article | Vol. 7, No. 9 | 1 Sept 2016 | BIOMEDICAL OPTICS EXPRESS 3247

Biomedical Optics EXPRESS

Dark field optical imaging reveals vascular changes in an inducible hamster cheek pouch model during carcinogenesis

FANGYAO HU, ROBERT MORHARD, HELEN A. MURPHY, CAIGANG ZHU, AND NIMMI RAMANUJAM*

Department of Biomedical Engineering, Duke University, Durham, NC 27708, USA
**nimmi@duke.edu*

Abstract: In this study, we propose a low-cost cross-polarized dark field microscopy system for *in vivo* vascular imaging to detect head and neck cancer. A simple-to-use Gabor-filter-based image processing technique was developed to objectively and automatically quantify several important vascular features, including tortuosity, length, diameter and area fraction, from vascular images. Simulations were performed to evaluate the accuracies of vessel segmentation and feature extraction for our algorithm. Sensitivity and specificity for vessel segmentation of the Gabor masks both remained above 80% at all contrast levels when compared to gold-standard masks. Errors for vascular feature extraction were under 5%. Moreover, vascular contrast and vessel diameter were identified to be the two primary factors which affected the segmentation accuracies. After our algorithm was validated, we monitored the blood vessels in an inducible hamster cheek pouch carcinogen model over 17 weeks and quantified vascular features during carcinogenesis. A significant increase in vascular tortuosity and a significant decrease in vessel length were observed during carcinogenesis.

©2016 Optical Society of America

OCIS codes: (170.0170) Medical optics and biotechnology; (170.0180) Microscopy; (170.3880) Medical and biological imaging; (170.4730) Optical pathology.

References and links

1. NIH, "https://costprojections.cancer.gov/graph.php," (2010).
2. J. Ferlay, I. Soerjomataram, R. Dikshit, S. Eser, C. Mathers, M. Rebelo, D. M. Parkin, D. Forman, and F. Bray, "Cancer incidence and mortality worldwide: sources, methods and major patterns in GLOBOCAN 2012," Int. J. Cancer **136**(5), E359–E386 (2015).
3. "Winning the Battle Against Head and Neck Cancer" (Seattle Cancer Care Alliance), retrieved http://www.seattlecca.org/diseases/head-neck-cancer-survival-rates.cfm.
4. J. Folkman, D. M. Long, Jr., and F. F. Becker, "Growth and Metastasis of Tumor in Organ Culture," Cancer **16**(4), 453–467 (1963).
5. M. J. Folkman, D. M. Long, Jr., and F. F. Becker, "Tumor growth in organ culture," Surg. Forum **13**, 81–83 (1962).
6. M. Sathyakumar, G. Sriram, T. Saraswathi, and B. Sivapathasundharam, "Immunohistochemical evaluation of mast cells and vascular endothelial proliferation in oral precancerous lesion-leukoplakia," J. Oral Maxillofac. Pathol. **16**(3), 343–348 (2012).
7. Y. Jin, G. L. Tipoe, F. H. White, and L. Yang, "A quantitative investigation of immunocytochemically stained blood vessels in normal, benign, premalignant and malignant human oral cheek epithelium," Virchows Arch. **427**(2), 145–151 (1995).
8. V. T. C. Chang, P. S. Cartwright, S. M. Bean, G. M. Palmer, R. C. Bentley, and N. Ramanujam, "Quantitative Physiology of the Precancerous Cervix in Vivo Through Optical Spectroscopy," Neoplasia **11**(4), 325–332 (2009).
9. R. H. Farnsworth, M. Lackmann, M. G. Achen, and S. A. Stacker, "Vascular remodeling in cancer," Oncogene **33**(27), 3496–3505 (2014).
10. C. Blatter, J. Weingast, A. Alex, B. Grajciar, W. Wieser, W. Drexler, R. Huber, and R. A. Leitgeb, "In situ structural and microangiographic assessment of human skin lesions with high-speed OCT," Biomed. Opt. Express **3**(10), 2636–2646 (2012).
11. R. Reif and R. K. Wang, "Label-free imaging of blood vessel morphology with capillary resolution using optical microangiography," Quant. Imaging Med. Surg. **2**(3), 207–212 (2012).
12. E. M. C. Hillman, A. Devor, A. K. Dunn, and D. A. Boas, "Laminar optical tomography: high-resolution 3D functional imaging of superficial tissues - art. no. 61431M," P Soc Photo-Opt Ins 6143, M1431–M1431 (2006).

#267830 http://dx.doi.org/10.1364/BOE.7.003247
Journal © 2016 Received 9 Jun 2016; revised 22 Jul 2016; accepted 22 Jul 2016; published 5 Aug 2016

Biomedical Optics EXPRESS

13. H. Sherman, S. Klausner, and W. A. Cook, "Incident dark-field illumination: a new method for microcirculatory study," Angiology **22**(5), 295–303 (1971).
14. K. R. Mathura, G. J. Bouma, and C. Ince, "Abnormal microcirculation in brain tumours during surgery," Lancet **358**(9294), 1698–1699 (2001).
15. F. Feldchtein, V. Gelikonov, R. Iksanov, G. Gelikonov, R. Kuranov, A. Sergeev, N. Gladkova, M. Ourutina, D. Reitze, and J. Warren, "In vivo OCT imaging of hard and soft tissue of the oral cavity," Opt. Express **3**(6), 239–250 (1998).
16. S. F. Chen, C. W. Lu, Y. M. Wang, M. T. Tsai, and C. C. Yang, "In vivo OCT imaging of the oral cavity tissue by use of a probe," 2005 Pacific Rim Conference on Lasers and Electro-Optics, 198–199 (2005).
17. P. K. Upputuri, K. Sivasubramanian, C. S. K. Mark, and M. Pramanik, "Recent Developments in Vascular Imaging Techniques in Tissue Engineering and Regenerative Medicine," BioMed Res. Int. **2015**, 783983 (2015).
18. W. Groner, J. W. Winkelman, A. G. Harris, C. Ince, G. J. Bouma, K. Messmer, and R. G. Nadeau, "Orthogonal polarization spectral imaging: A new method for study of the microcirculation," Nat. Med. **5**(10), 1209–1212 (1999).
19. M. Heger, J. Beek, K. Stenback, D. Faber, M. van Gemert, and C. Ince, "Darkfield orthogonal polarized spectral imaging for studying endovascular laser-tissue interactions in vivo - a preliminary study," Opt. Express **13**(3), 702–715 (2005).
20. S. Andrejevic, J. F. Savary, C. Fontolliet, P. Monnier, and H. van Den Bergh, "7,12-Dimethylbenz[a]anthracene-induced 'early' squamous cell carcinoma in the Golden Syrian hamster: Evaluation of an animal model and comparison with 'early' forms of human squamous cell carcinoma in the upper aero-digestive tract," Int. J. Exp. Pathol. **77**(1), 7–14 (1996).
21. X. Liu, Y. Huang, and J. U. Kang, "Dark-field illuminated reflectance fiber bundle endoscopic microscope," J. Biomed. Opt. **16**(4), 046003 (2011).
22. S. Preibisch, S. Saalfeld, and P. Tomancak, "Globally optimal stitching of tiled 3D microscopic image acquisitions," Bioinformatics **25**(11), 1463–1465 (2009).
23. R. Estrada, C. Tomasi, M. T. Cabrera, D. K. Wallace, S. F. Freedman, and S. Farsiu, "Exploratory Dijkstra forest based automatic vessel segmentation: applications in video indirect ophthalmoscopy (VIO)," Biomed. Opt. Express **3**(2), 327–339 (2012).
24. F. Farokhian and H. Demirel, "Blood Vessels Detection and Segmentation in Retina using Gabor Filters," 2013 10th International Conference on High Capacity Optical Networks and Enabling Technologies (Honet-Cns), 104–108 (2013).
25. S. K. Kuri and M. R. Hossain, "Automated Retinal Blood Vessels Extraction Using Optimized Gabor Filter," 2014 International Conference on Informatics, Electronics & Vision (Iciev) (2014).
26. M. Nandy and M. Banerjee, "Retinal Vessel Segmentation Using Gabor Filter and Artificial Neural Network," Proc Int Conf Emerg, 157–160 (2012).
27. C. Heneghan, J. Flynn, M. O'Keefe, and M. Cahill, "Characterization of changes in blood vessel width and tortuosity in retinopathy of prematurity using image analysis," Med. Image Anal. **6**(4), 407–429 (2002).
28. X. R. Bao, X. Ge, L. H. She, and S. Zhang, "Segmentation of retinal blood vessels based on cake filter," BioMed Res. Int. **2015**, 137024 (2015).
29. J. V. K. Saumitra Kumar Kuri, "Automated Segmentation of Retinal Blood Vessels using Optimized Gabor Filter with Local Entropy Thresholding," Int. J. Comput. Appl. **114**, 37–42 (2015).
30. S. Goel, D. G. Duda, L. Xu, L. L. Munn, Y. Boucher, D. Fukumura, and R. K. Jain, "Normalization of the Vasculature for Treatment of Cancer and Other Diseases," Physiol. Rev. **91**(3), 1071–1121 (2011).
31. C. Y. Li, S. Shan, Q. Huang, R. D. Braun, J. Lanzen, K. Hu, P. Lin, and M. W. Dewhirst, "Initial stages of tumor cell-induced angiogenesis: Evaluation via skin window chambers in rodent models," J. Natl. Cancer Inst. **92**(2), 143–147 (2000).
32. L. Conroy, R. S. DaCosta, and I. A. Vitkin, "Quantifying tissue microvasculature with speckle variance optical coherence tomography," Opt. Lett. **37**(15), 3180–3182 (2012).
33. S. E. Shelton, Y. Z. Lee, M. Lee, E. Cherin, F. S. Foster, S. R. Aylward, and P. A. Dayton, "Quantification of Microvascular Tortuosity during Tumor Evolution Using Acoustic Angiography," Ultrasound Med. Biol. **41**(7), 1896–1904 (2015).
34. A. G. Lurie, M. Tatematsu, T. Nakatsuka, R. M. Rippey, and N. Ito, "Anatomical and Functional Vascular Changes in Hamster Cheek Pouch during Carcinogenesis Induced by 7, 12-Dimethylbenz(a)Anthracene," Cancer Res. **43**(12 Pt 1), 5986–5994 (1983).
35. P. T. Goedhart, M. Khalilzada, R. Bezemer, J. Merza, and C. Ince, "Sidestream Dark Field (SDF) imaging: a novel stroboscopic LED ring-based imaging modality for clinical assessment of the microcirculation," Opt. Express **15**(23), 15101–15114 (2007).
36. F. Farahmand, K. Eftekhari, V. Modarresi, M. Najafi-Sani, A. Khodadad, and F. Motamed, "Comparing Oral Route Paraffin Oil versus Rectal Route for Disimpaction in Children with Chronic Constipation; a Randomized Control Trial," Iran. J. Pediatr. **20**(3), 291–296 (2010).
37. A. L. Harris, "Hypoxia--A key regulatory factor in tumour growth," Nat. Rev. Cancer **2**(1), 38–47 (2002).
38. F. Hu, K. Vishwanath, H. Wolfgang Beumer, L. Puscas, H. R. Afshari, R. M. Esclamado, R. Scher, S. Fisher, J. Lo, C. Mulvey, N. Ramanujam, and W. T. Lee, "Assessment of the sensitivity and specificity of tissue-specific-based and anatomical-based optical biomarkers for rapid detection of human head and neck squamous cell carcinoma," Oral Oncol. **50**(9), 848–856 (2014).

Biomedical Optics EXPRESS

39. F. Hu, K. Vishwanath, J. Lo, A. Erkanli, C. Mulvey, W. T. Lee, and N. Ramanujam, "Rapid Determination of Oxygen Saturation and Vascularity for Cancer Detection," PLoS One **8**(12), e82977 (2013).
40. J. Y. Lo, J. Q. Brown, S. Dhar, B. Yu, G. M. Palmer, N. M. Jokerst, and N. Ramanujam, "Wavelength Optimization for Quantitative Spectral Imaging of Breast Tumor Margins," PLoS One **8**(4), e61767 (2013).
41. M. Khalilzada, K. Dogan, C. Ince, and J. Stam, "Sublingual Microvascular Changes in Patients With Cerebral Small Vessel Disease," Stroke **42**(7), 2071–2073 (2011).

1. Introduction

The NIH predicts that there will be approximately 50,000 new head and neck cancers in 2016 in the U.S. and the estimated cost spent on head and neck cancer care will be around $ 4.0 billion [1]. The incidence of head and neck cancer is much worse in low- and middle-income countries (LMICs). Approximately 1 million new head and neck cancer cases are expected in LMICs each year according to the most recent cancer facts and Figs [2]. Based on the report from the National Cancer Data Base, the 5-year survival rate is 77% if head and neck cancer is diagnosed at stage I while the 5-year survival rate is nearly cut in half if it is diagnosed at stage IV [3]. Early diagnosis of head and neck cancer is important to improve the cost-benefit ratio of health care delivery in the U.S. and in LMICs where there are limited resources for cancer treatment. Therefore, a simple-to-use and low-cost technique is needed that can be used by non-specialists and can effectively diagnose lesions at their pre-cancerous stage such that relatively low-cost interventions can be made early in the course of the disease.

Neovascularization is particularly important for cancer development as the size of the tumor is limited to 1-2 mm before the onset of angiogenesis, also known as activating the angiogenic switch [4, 5]. Once the angiogenic switch is activated, neovascularization will form around hypoxic regions to provide adequate oxygen and nutrition supply to fuel tumor growth. This proliferation of vasculature can be quantified via an increase in microvessel density and is observed in precancerous and cancerous lesions [6–8]. However, few studies have utilized *in vivo* vascular morphology for the detection of head and neck pre-cancers. Unlike neovascularization in the normal wound healing process, the tumor-induced neovasculature is highly disorganized, leaky, tortuous and dilated [9]. Thus, quantitative imaging of neovascularization can be an effective means to detect head and neck pre-cancers.

Several label-free optical techniques including optical coherence tomography (OCT) [10, 11], laminar optical tomography (LOT) [12], dark field (DF) microscopy [13] and cross-polarized (CP) microscopy [14], have been explored for non-invasive vascular imaging *in vivo*. OCT provides label-free high-resolution (several microns) vascular imaging using the laser Doppler Effect resulting from moving blood cells. The sensing depth for OCT in oral mucosal tissues is about 900 μm with a 950 nm laser [15, 16]. LOT utilizes Monte Carlo modeling, scanning mirrors, and optical fibers to reconstruct depth sensitive (~2 mm) vascular images with sub-millimeter resolution. Both DF and CP are simple techniques to image vasculature *in vivo*. DF and CP microscopy can provide micron resolution images of the vasculature in the oral cavity with a sensing depth of up to 1 mm [17, 18]. DF microscopy is sensitive to back scattered light while effectively rejecting tissue specular reflection simply by re-designing different illumination and collection paths with the help of a stop and iris. CP microscopy only collects light with orthogonal polarization. Therefore, specular reflection is unlikely to be collected since its polarization state is the same as the illuminating light. Heger et al. combined CP and DF techniques and demonstrated that CPDF technique showed superior vascular contrast than CP technique alone [19]. To determine which technique is more suited for LMICs application, we summarized the cost of the critical components for typical OCT, LOT and CPDF microscope systems (Table 1). Prices were estimated from Thorlab, Prixmatix and Melles Griot. Due to the low-cost nature and the simplicity of system designs for CPDF microscopy, we chose to investigate carcinogenesis associated vascular changes using CPDF microscopy.

Biomedical Optics EXPRESS

Table 1. Estimated cost for the critical components of optical coherence tomography, laminar optical tomography and cross-polarized dark field microscopy.

	OCT		LOT		CPDF microscopy	
Source	Swept source laser	$35,000	DPSS laser	$6,000	LED module	$2,000
Detector	DBD	$1,550	7 APD	$8,000	CMOS camera	$350
Objective lens	5X Scan lens	$900	4.6X Scan lens	$900	4X Plan Achromat	$200
Other critical components	Galvo system	$2,400	2 Galvo systems	$4,800	stop and iris	$100
Total		$39,850		$19,700		$2,650

(DBD: Dual balanced detector, DPSS: Diode-pumped solid-state, APD: Avalanche photodiode detector).

In this study, we developed a low-cost and label-free technique, i.e. cross-polarized dark field microscopy (CPDF-microscopy), to image neovascularization changes associated with pre-cancer and cancer development. Vascular images were processed with a Gabor algorithm to objectively and automatically extract vascular features. Simulations were performed to evaluate the accuracies of the vessel segmentation and feature extraction. Sensitivity and specificity for vessel segmentation of the Gabor masks both remained above 80% and errors for vascular feature extraction were under 5%. Moreover, vascular contrast and vessel diameter were identified to be the two primary factors which affected the segmentation accuracies. After the accuracies of our algorithm were evaluated, we monitored the blood vessels in an inducible hamster cheek pouch tumor model, a well-established inducible model for head and neck cancer [20], during the 17 weeks of tumor inducement. Vascular tortuosity and length in the control and the carcinogen treated cheek pouches follow significantly different trends through malignant transformation. Our results suggest that monitoring vascular features with a low-cost CPDF-microscopy is a promising approach for head and neck pre-cancer detection in LMICs.

2. Materials and methods

2.1. Dark field microscope system design

The system design was inspired by Liu et al [21]. A detailed schematic of our CPDF microscopy system is shown in Fig. 1. A white light LED source (Prizmatix, UHP-T-LED-White, Southfield, MI, USA) was used to provide illumination with a band of 400 - 700 nm. In the illumination channel, the light from the LED was coupled into an optical fiber with a diameter of 1000 μm and an NA of 0.39 (M35L01, Thorlab, USA) first and then collimated with an aspherized achromatic lens (Edmund, f = 30 mm). An optical stop was used to create a ring beam before the light beam was delivered into a polarization-insensitive beam splitter (Edmund). A 4X objective lens (Olympus, plan achromat) with an NA of 0.1 was used to deliver the ring beam to the sample. In the detection channel, an iris was placed next to the beam splitter to block the specular reflection. An achromatic lens (Thorlab, AC254-150-A-ML) was placed next to the iris to form the image of the backscattered light from the sample onto a CMOS RGB camera (Thorlab, DCC1645C). The specular reflection from the tissue surface can be effectively rejected by optimizing the iris and stop size such that the iris diameter was slightly smaller than the stop diameter. The diameters of the stop and iris were 8 mm and 6 mm, respectively. A polarizer and an analyzer (Edmund, linear glass polarizers) were used to reject the scattered light from the uneven surface of sample. Therefore, only the diffuse reflectance from the sample was detected. The final resolution for the CPDF measured from a resolution target was 3.1 μm and the measured field of view (FOV) was 1.5 mm by 1.0 mm. A total of 0.324 mW/cm^2 at 540 nm was delivered to the sample. The power spectrum of the LED source is shown in Fig. 1. The entire system was controlled via a custom designed LabVIEW program.

Biomedical Optics EXPRESS

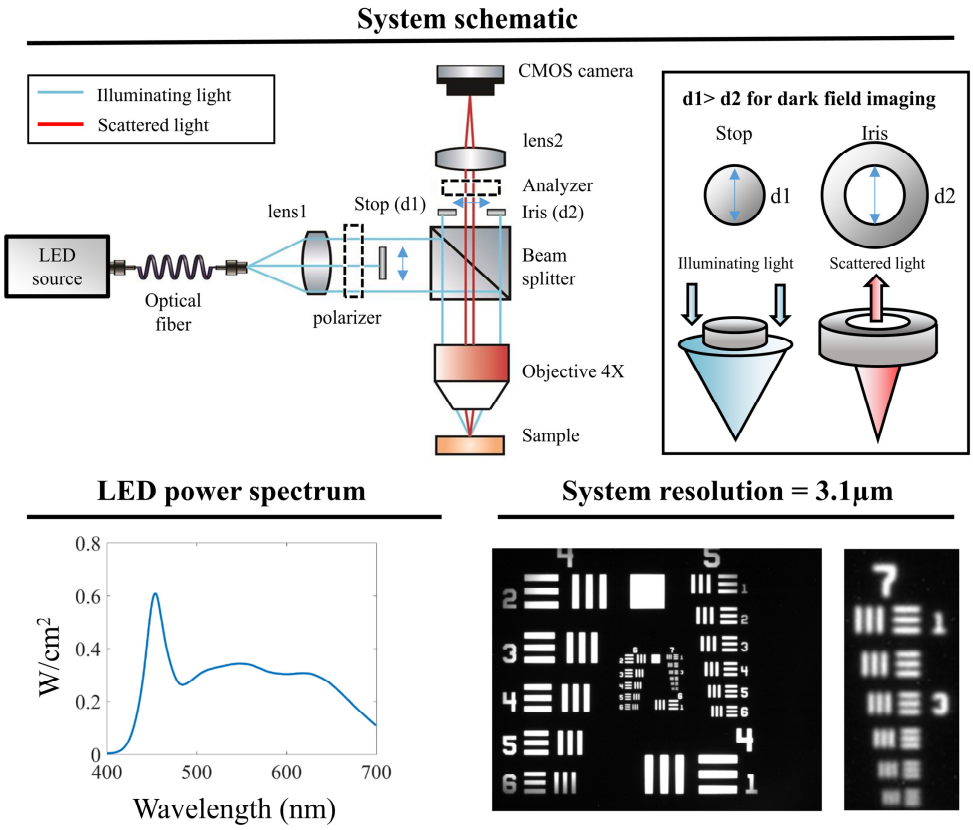

Fig. 1. Schematic of the dark field microscope system and the measured resolution. The key components in the cross-polarized dark field microscopy system are the stop and iris, which are 8mm and 6mm, respectively. They remove specular reflectance while maintaining high contrast for the detected diffuse reflectance. Cross polarized imaging was achieved by placing a polarizer in the illumination channel and an analyzer in the collection channel. The power spectrum is shown. The measured resolution is 3.1 µm. The measured field of view is 1.5 mm by 1 mm.

2.2. Imaging study design in a hamster cheek pouch carcinogen model

The animal study protocol was approved by the Duke University Institutional Animal Care and Use Committee. A total of 14 Golden Syrian hamsters were used in the study. A paint brush was dipped in 0.5% (by weight) dimethylbenz[a]anthracene (DMBA)-mineral oil solution and then applied to the entire cheek pouches. For each hamster, the right cheek pouch was treated with DMBA-mineral oil solution three times per week for a total of 17 weeks. The left cheek pouch (control cheek) was treated at the same frequency with mineral oil only. The study timeline is shown in Fig. 2.

Biomedical Optics EXPRESS

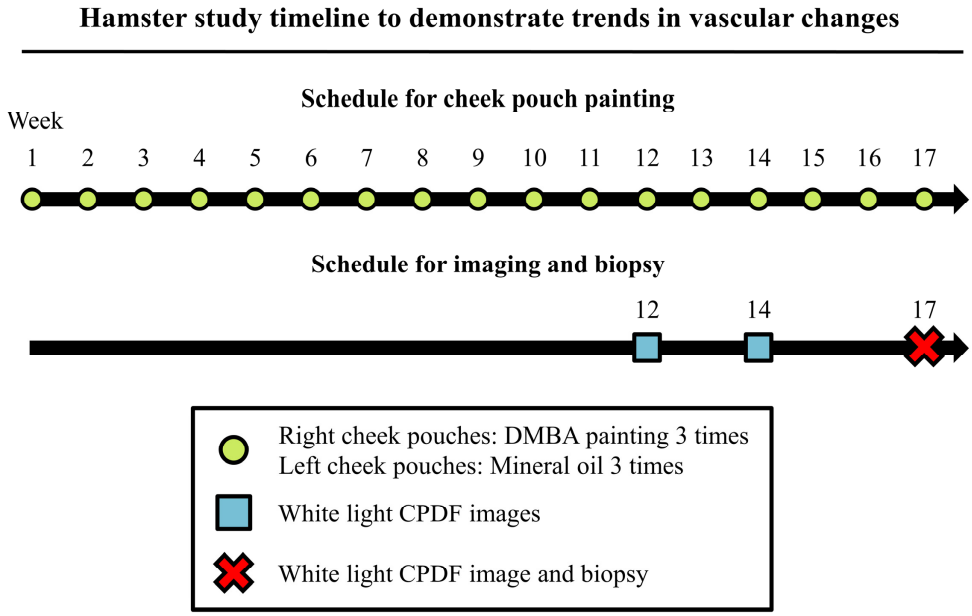

Fig. 2. Timeline and endpoints for the hamster study design. To demonstrate the ability of our dark field system to monitor *in vivo* vascular changes during carcinogenesis in an inducible cancer model, non-invasive cross-polarized dark field (CPDF) images were obtained from hamster cheek pouches at week 12, 14 and 17 after treatment with dimethylbenz[a]anthracene (DMBA). Biopsies were obtained at week 17 from the sites that were imaged to confirm the induction of cancer.

During optical imaging, animals were placed on a heating pad to maintain their body temperature under general anesthesia. A random location of the cheek pouch was stretched over a 14 mm (diameter) plastic post. A 3 × 3 image mosaic was obtained at the center of the post for each cheek pouch. The exposure times ranged from 900 to 5000 ms for the CPDF imaging depending on camera saturation. Each image mosaic was composed of 9 CPDF images and the field of view (FOV) was approximately 3.2 by 2.7 mm. Image mosaics were obtained at week 12, 14 and 17 from all animals for both cheek pouches. Biopsies and corresponding pathology was obtained at the site of imaging at week 17 for both DMBA treated and control cheek pouches. The invasive nature of biopsying the cheek pouch would damage the tissues and might alter our observation. Therefore, biopsy was only performed at week 17 immediately prior to euthanasia and pathology was only available for week 17. All images were processed with the algorithm described in the next section.

2.3. Image processing and vascular feature quantification

The image processing was performed according to the following procedure. For each cheek pouch, the first step is to stitch the 9 CPDF images to increase the FOV. Image stitching was performed with ImageJ [22] Once the images were stitched, they were down scaled in size by 0.25 using a bicubic interpolation to reduce the computational time. Next, the green channel of the stitched image was divided by its red channel (G/R image). All pixels with an intensity greater than 1 was set to 1 in the G/R images. Further, the scale of the G/R image was reversed by 1 - G/R image (reverse G/R image). To objectively evaluate the vasculature, a Gabor algorithm was applied to the reverse G/R images to segment the vasculature [23]. In short, a multi-scale Gabor filter with different orientations (0, 22.5, 45, 67.5, 90, 112.5, 135 and 157.5 degree) was convolved with the reverse G/R images to obtained the overall Gabor responses. Studies used different orientations of the Gabor filter to compute the Gabor

Biomedical Optics EXPRESS

responses of vascular images [24–26]. The orientations used in this study are the same as in previous studies [23]. Next, Dijkstra forest vessel segmentation algorithm was used to generate the binary vessel mask from the Gabor responses. The algorithm starts with the pixel with the highest Gabor response and progressively explores the rest of the image to determine if the pixel is in the vascular area or not.

Once the image was processed by the Gabor algorithm [23], a binary vessel mask was obtained for each reverse G/R image. Area fraction was computed by dividing the sum of the vascular pixels to the total field of view of the binary vessel mask. To quantify other vascular features, the binary mask was further skeletonized from which the vessel branch points and end points were identified. Based on the skeletonized image, vascular tortuosity, length and diameter were computed. The methods to compute the vascular length and tortuosity are described by Heneghan et al [27]. In short, the vascular length (d_{curve}) is the distance that a vessel segment traveled and d_{curve} and was computed from summing the number of pixels in each vessel segment. The tortuosity was computed from dividing d_{curve} by the Euclidean distance of its two ends. Vessel diameter was determined with the distance transform of the binary mask.

2.4. Simulation to investigate the impact of vascular contrast on segmentation accuracies and extraction of vascular parameters

Vascular contrast can vary between images, especially during carcinogenesis. It is important to understand how vascular contrast affects the performance of the Gabor algorithm for blood vessel segmentation. Therefore, we simulated vascular images with various levels of contrast and used the Gabor algorithm to segment vessels in the simulated images. To generate the gold-standard masks and provide the simulation with proper noise levels in the non-vascular areas, 10 reverse G/R images were randomly selected from the study (4 images from control hamsters at week 12 and 2 images from DMBA treated cheek pouches at week 12, 14 and 17 respectively). Vessels in the 10 selected images were manually traced to generate the gold-standard masks. The gold-standard masks are binary masks which indicate whether each pixel is either in the vascular area or not. The noise levels were estimated by computing the mean and variance in intensity of the non-vascular area in the reverse G/R images using the information of the gold-standard masks. The computed mean intensity for the non-vascular area were 0.38 and 0.51 for the 4 and 6 selected images from the control and DMBA treated cheek pouches respectively. The computed variance in intensity for the non-vascular area were 0.0108 and 0.0152 for the 4 and 6 selected images from the control and DMBA treated cheek pouches respectively. The overall mean and variance in intensity for the non-vascular area were 0.44 and 0.014.

The details of the simulation are described below. All gold-standard masks (contrast = 1) were used in the simulation and each gold-standard mask was used to generate a set of simulated images. First, the intensities of the vascular area were assigned a constant value of 1 and the non-vascular area was assigned a constant value of 0 for the gold-standard mask. Second, Gaussian noise (with mean of 0.44 and variance of 0.014) was added to the gold-standard mask to generate a simulated image with noise. Third, contrast in the simulated image was varied from 0.05, 0.15, 0.25 … to 0.75 in steps of 0.1. Contrast was defined as the difference between the average intensity in the vascular area and in the non-vascular area.

Next, the Gabor algorithm was used to segment the vessels in the simulated images and binary Gabor masks were generated. Finally, pixel-wise comparisons were made between the Gabor masks and the gold-standard mask. Specifically, every pixel in the Gabor mask was compared to the corresponding pixel at the in the gold-standard mask. Each pixel was then classified as a true positive (TP), false positive (FP), true negative (TN) or a false negative (FN) pixel. TP pixels are the pixels in the vascular area for both gold-standard masks and Gabor masks whereas FP pixels are those in the vascular area for Gabor masks but in the non-vascular area of the gold-stand masks. Similarly, TN pixels are the pixels in the non-vascular

Biomedical Optics EXPRESS

area for both Gabor masks and gold-standard mask. FN pixels are the pixels in the non-vascular area of the Gabor masks but in the vascular area of the gold-standard masks. Table 2 summarizes the definition of TP,TN,FP and FN. Sensitivities and specificities were computed from the number of pixels for TP, FP, TN and FN. Sensitivity is the ratio of TP to the sum of TP and FN and the specificity is the ratio of TN to the sum of TN and FP.

Table 2. Definition of true positive, true negative, false positive and false negative for vessel classification.

	Vessel present (gold standard)	Vessel absent (gold standard)
Vessel detected	True positive (TP)	False positive (FP)
Vessel not detected	False negative (FN)	True negative (TN)

To evaluate the accuracy of the method for blood vessel features quantification, a simple simulation study was performed. Specifically, 3 vascular images were created. In each image, 6 blood vessels were generated. Each blood vessel was a simple sinusoidal curve of the form $A \sin\theta$. The vessels were assigned a constant intensity of 0.65 and Gaussian noise (mean: 0.44, variance: 0.01) was assigned to the non-vascular area. The intensity value of 0.65 is the average intensity in the vascular area from the selected images in previous sections. In each image, the tortuosity of the 6 blood vessels was varied (1.01, 1.04, 1.07, 1.12, 1.18 and 1.24) by varying the arc-length (2.54, 2.60, 2.68, 2.78, 2.91 and 3.10 mm) but the diameter was kept the same in each image. The diameters of the vessels in the 3 images were 20 µm, 200 µm and 400 µm (5, 50 and 100 pixels). The Gabor algorithm was used to segment the vessels in the 3 simulated images. Tortuosity, diameter and vascular length were computed from the Gabor masks. The estimated vascular features were compared with the gold-standard values to compute the percent errors in extracting tortuosity, diameter and length respectively.

2.5. Performance of Gabor algorithm in the hamster cheek pouch model

To estimate the contrast and the performance of the Gabor algorithm on the hamster cheek pouch model images, the same 10 randomly selected reverse G/R images in the previous section and their corresponding gold-standard masks were used. The vascular area and the non-vascular area were indicated by the corresponding gold-standard mask for each selected image. Average contrast for each selected image was computed by calculating the difference between the average intensity in the vascular area and the non-vascular area. Sensitivity and specificity were computed by comparing the corresponding gold-standard masks and the Gabor masks for the 10 selected images respectively. The results were first stratified by DMBA treatment and then averaged based on the week the images were collected.

The average vascular area fraction, tortuosity, diameter and length for all hamsters at all time points were computed from the Gabor masks. A non-parametric repeated measure model (Friedman test) was used to compare the average vascular features between the DMBA treated and control cheeks during the study. The average vascular features at week 17 between the cheek pouches which were diagnosed as normal or squamous cell carcinoma (SCC) were compared using Wilcoxon signed-rank test. All statistical analyses were performed using MATLAB.

3. Results

A total of 11 DMBA treated hamster cheek pouches were diagnosed as SCC at week 17. Two hamsters' DMBA treated cheek pouches were diagnosed as dysplasia at week 17 and one hamster's DMBA treated cheek pouch was diagnosed as hyperplasia at week 17. The hamsters with dysplasia and hyperplasia were excluded from the analyses due to the small sample size. All of the control cheek pouches were diagnosed as normal. Figure 3(a) shows a representative example of the image processing steps performed on one control and one DMBA treated cheek pouch image obtained at week 12 from the same hamster. Representative time course reverse G/R images and Gabor masks from another hamster are

Biomedical Optics EXPRESS

shown in Fig. 3(b) and Fig. 3(c) respectively. Vascular features in the normal and SCC cheek pouches are visually distinguishable as shown in Fig. 3(b) and Fig. 3(c).

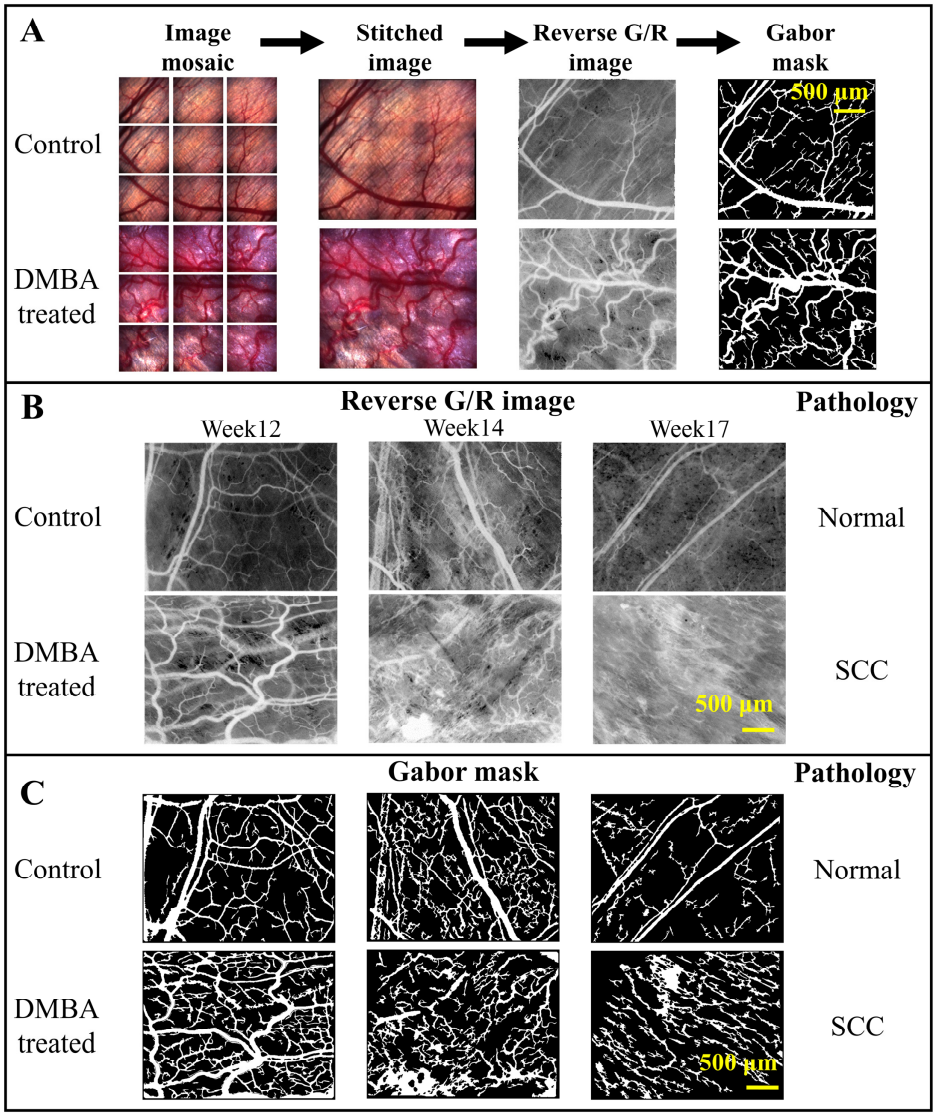

Fig. 3. Representative images of the steps to obtain a Gabor mask from the raw images and the representative time course reverse G/R images obtained during the study. (A) A 3 by 3 image mosaic was obtained and stitched. The Gabor algorithm was applied to the reverse G/R image to obtain the Gabor mask. (B) The images depict the progression of a single cheek pouch from week 12 to week 17 of mineral oil or DMBA treatment. Pathology was confirmed for the image site at week 17. Pathology was not available at week 12 and 14 at the image sites since biopsy would damage the tissues and might alter our observation. (C) The corresponding Gabor masks are also shown. SCC: squamous cell carcinoma.

3.1. Vascular contrast affect segmentation accuracies

Figure 4(a) shows the representative simulated vascular images and the corresponding mask validation. The TP, FP and FN pixels were color-coded in the validation images. The Gabor algorithm failed to identify smaller vessels when the contrast is low, as shown in the validation images with contrast of 0.05. The contrast dependence of the computed sensitivities

Biomedical Optics EXPRESS

and specificities is shown in Fig. 4(b). The sensitivity increased with an increase in vascular contrast for both control and DMBA treated cheek pouch images. The specificity remained above 90% even when the contrast was 0.05. There is no noticeable difference in segmentation accuracy between normal and DMBA-treated groups as the average difference in sensitivity and specificity from all contrast levels were only 0.66% and 0.61%, respectively (Fig. 4(b)). These results suggest that contrast is the primary factor that affects the segmentation accuracy.

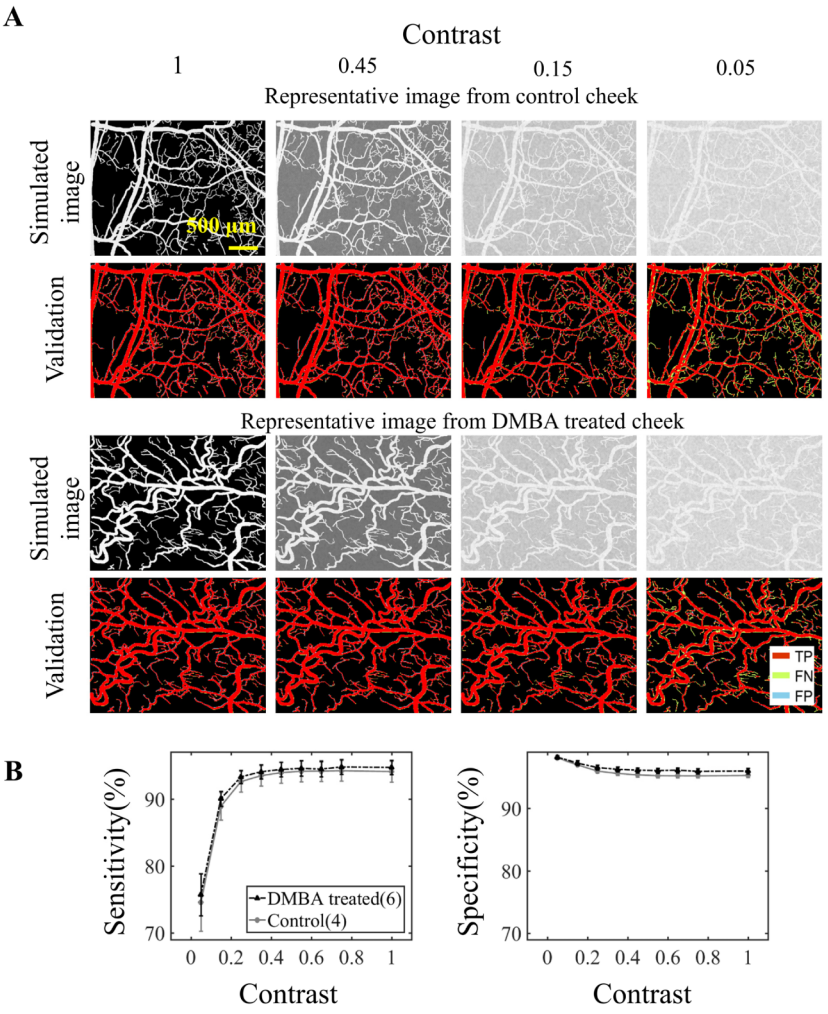

Fig. 4. Gabor filter vascular segmentation accuracy is affected by vascular contrast. (A) Vascular images with varying levels of vascular contrast were simulated. Vascular contrast was defined as the difference between the average intensity in the vascular area and the average intensity in the non-vascular area. A total of 10 randomly selected hamster cheek pouches images (N = 4 for control from week 12, N = 2 for DMBA treated cheek pouch from week 12, 14 and 17 respectively) were used for the simulation. Representative simulated images and their corresponding validation are shown. The Gabor filter was used to segment the vasculature in the simulated images. The segmented masks were compared to the original gold-standard mask. True positive (TP), false negative (FN) and false positive (FP) pixels are identified and color-coded. (B) The computed sensitivities and specificities for varying vascular contrast. Sensitivity increased with vascular contrast and specificity remained above 90% in the simulations. Error bars show standard error.

Biomedical Optics EXPRESS

3.2. Gabor algorithm overestimates diameter for small vessels

Figures 5(a), 5(b) and 5(c) shows the simulated vascular images, Gabor filter segmented mask and the corresponding percent errors of the extracted vascular endpoints respectively. The errors of the measured tortuosity and lengths were all within the 5% range. The errors of the measured diameters were all within 6% when the expected diameter was larger than 200 μm. The errors of the measured diameter went up to 15% when the diameter decreased to 30 μm (data not shown). The errors went above 50% when the expected diameter was less than 20 μm. These results demonstrate that the Gabor algorithm failed in extracting small features in the vascular images.

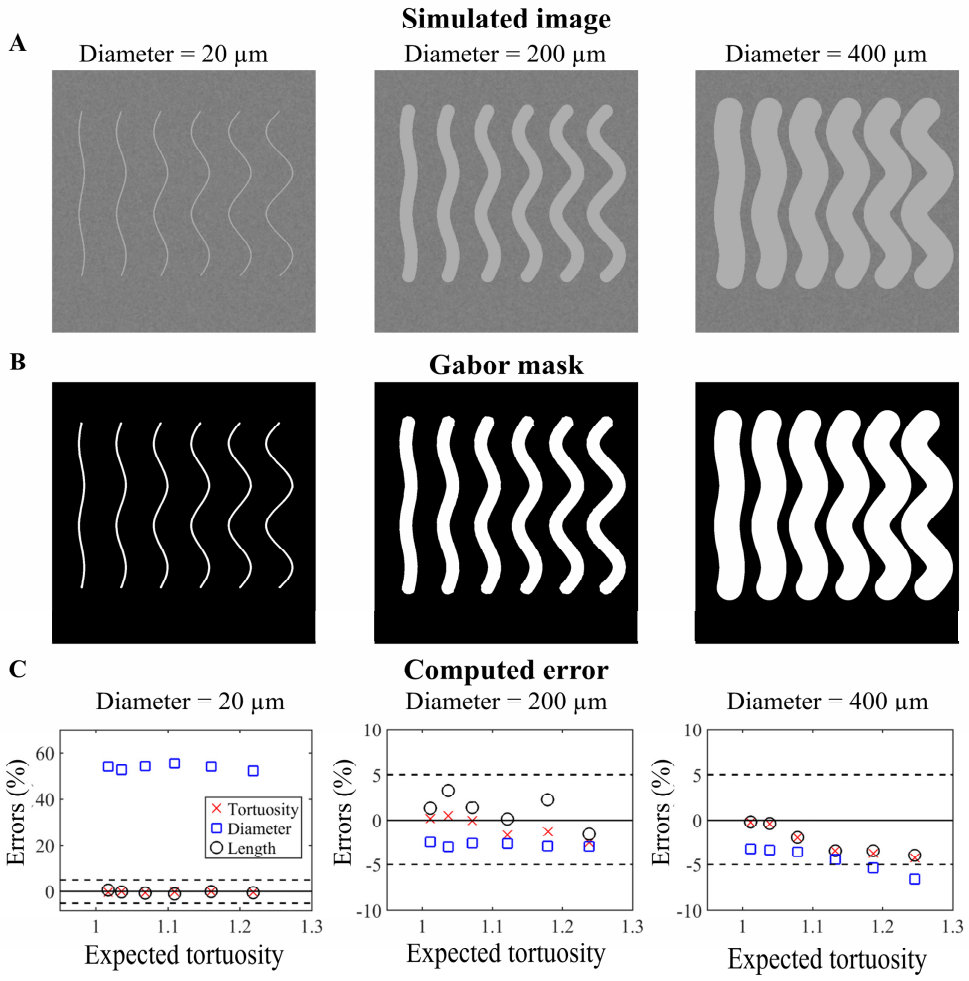

Fig. 5. The Gabor algorithm overestimated the vascular diameter of the small vessels. (A) Simulated vascular images with different diameters and tortuosities. (B) Gabor masks derived from the simulated vascular images. (C) Tortuosity, diameter and length were computed from the Gabor masks. Gabor algorithm overestimated the vascular diameter more than 50% when the vascular diameter were 20 μm. The errors of the extracted diameters were within 6% when the expected diameters were 200 or 400 μm. The errors of the extracted tortuosity and length were all within 5% when the expected diameters were 20, 200 or 400 μm. Dash lines show the 5% and −5% boundaries.

Biomedical Optics EXPRESS

3.3. Gabor algorithm segmented vasculature with high accuracy

Figure 6(a) shows representative reverse G/R images, manually traced masks, Gabor masks and the corresponding mask validation. The TP, FP and FN pixels were color-coded in the validation images. Figure 6(b) shows the sensitivity and specificity for the 4 control and 6 DMBA treated cheek pouches. The sensitivity and specificity were plotted against contrast, from which we can observe that the sensitivity increased with contrast while specificity remained above 80% for the 10 selected images.

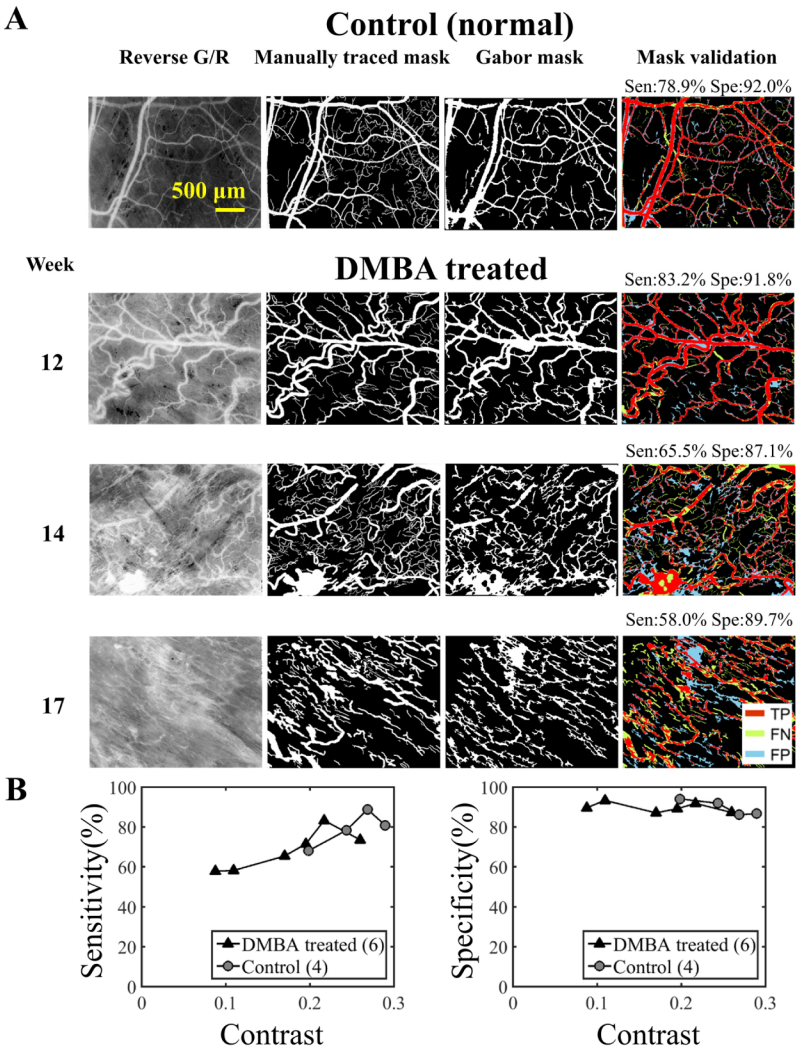

Fig. 6. Gabor algorithm segments the vasculature with high accuracies. (A) A total of 10 randomly selected hamster cheek pouches images (N = 4 for control from week 12, N = 2 for DMBA treated cheek pouch from week 12, 14 and 17 respectively) were used to validate the Gabor masks. Ten manually traced masks were used to validate the Gabor masks. The manually traced masks served as the gold standard. The sensitivity and specificity for identifying the vasculature were computed for each selected image. (B) Vascular contrast was computed using the manually traced mask. Contrast was defined as the difference between the average intensity in the vascular area and non-vascular area. Contrast vs. sensitivity and specificity are shown. Sensitivity increased with contrast while specificity remained above 80% for the 10 selected images. Note the highest contrast computed from the selected image is less than 0.3. TP: true positive, FN: false negative, FP: false positive.

Biomedical Optics EXPRESS

Table 3 summarizes the average sensitivity and specificity and the computed contrast for the selected control and the DMBA treated images. The average contrast of the DMBA treated cheek pouches were always lower than the contrast for the control cheek pouches. The average contrast of the DMBA treated cheek pouches decreased approximately by 0.1 from the week 12 images to week 14 images and remained relatively constant to week 17.

Table 3. Average sensitivity, specificity and contrast from the selected images.

	Sensitivity (%)	Specificity (%)	Contrast
Control (N = 4)	79.12	89.81	0.2501
DMBA treated (Total N = 6)			
Week12 (N = 2)	78.50	89.65	0.2386
Week14 (N = 2)	61.88	90.32	0.1397
Week17 (N = 2)	64.76	89.51	0.1415

3.4. Vascular tortuosity, and length changed significantly during DMBA treatment

Studies have shown that the Gabor filter has failed in characterizing small vessels [28, 29]. Our results are consistent with the existing literature and show that the Gabor algorithm overestimated the diameters when the vessel diameters were under 20 µm (Fig. 5), thus vessels with diameter under 20 µm were removed before calculating tortuosity, length and diameter calculations for the hamster cheek pouch data.

Figure 7 shows the trends in vascular features of the hamster cheek pouches during the study. Tortuosity and length computed from the DMBA treated cheek pouches and the control cheek pouches demonstrated significantly different trends ($p<0.01$ for both) over the course of 12 to 17 weeks. For the computed vascular parameters with pathological confirmation at week 17, tortuosity was significantly higher in the SCC group than in the normal group ($p<0.01$). Vessel length was significantly lower in the SCC group than in the normal group ($p< 0.01$).

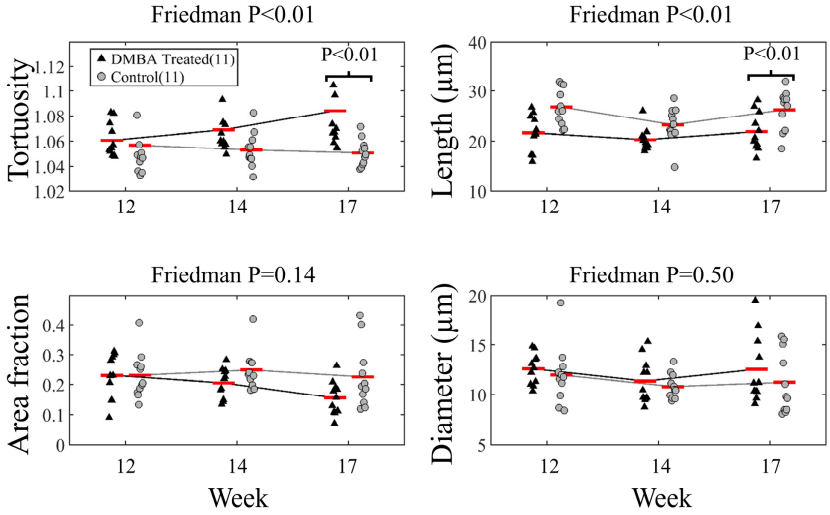

Fig. 7. Vascular tortuosity, length, area fraction and diameter were computed from DMBA treated and control cheek pouches during the study. Significant changes in vascular tortuosity and length were observed during DMBA treatment (Friedman test). DMBA treated cheek pouches demonstrated significantly different trends compared to the vascular features in the control cheek pouches during the study. In addition, Wilcoxon sign-rank tests were performed between the extracted vascular features from the DMBA treated and control cheek pouches at week 17.Tortuosity and length in the DMBA treated cheek pouches was significant higher and lower than the control cheeks at week 17. Red bars indicate the means.

Biomedical Optics EXPRESS

No significantly different trends were observed in tortuosity, area fraction and diameter when the small vessels were included. No significant differences between the SCC and the normal groups in tortuosity, area fraction and diameter at week 17 were observed when the small vessels were included. Vessel lengths in the DMBA treated cheek pouches still demonstrated significantly different trends compared to the control cheek pouches when the small vessels were included. Vessel lengths were also significantly lower in the SCC group than in the normal group at week 17 when the small vessel were included.

4. Discussion

We have demonstrated the capability of a simple-to-use and low-cost dark field microscope and Gabor filter based image processing algorithm to image and quantify vascular features in the hamster cheek pouch carcinogenesis model. For the first time, changes in vascular features associated with carcinogenesis in an inducible model were reported both noninvasively and quantitatively. DMBA treated cheek pouches show significantly different trends in tortuosity and length during the course of cancer development compared to those in control cheek pouches. Our results demonstrate the potential of using vascular features as an effective biomarker for cancer detection.

The measured vascular length in the DMBA treated cheek pouches were significantly lower than the measured length in the control cheek pouches at week 17 ($p<0.01$). The reason might be due to the increased neovascularization in the treated cheek pouch could lead to a reduction in average vascular length [30]. The trend of tortuosity from week 12 to week 17 in the DMBA treated hamster cheek pouches increased significantly when compared to the trend in the control cheek pouches ($p<0.01$). In addition, the tortuosity was significantly higher in the SCC group than the normal group ($p<0.01$) at week 17, which is consistent with the literature [30–32]. Li et al. observed a similar increase in vascular tortuosity in a mouse window chamber model [31]. Conroy et al. also demonstrated that tumor vasculature exhibited significantly higher tortuosity than control vasculature using an OCT techniques [32].

Both increases and decreases in vascular area fraction have been observed in tumors compared to normal tissues [30–33]. In our results (Fig. 7), vascular area fraction in the DMBA treated cheek pouches decreased by around 30% from week 12 to week 17 whereas the area fraction in the control cheek pouches remained unchanged. This was possibly due to hyperkeratinization and hyperplasia [20], which may decrease the visibility of the vasculature. Although the increased neovascularization could increase the vascular area fraction, hyperkeratinization and hyperplasia could reduce the visibility of the vessels thus reducing the overall vascular area fraction. Finally, diameters were not statistically different for the DMBA treated and the control cheek pouches although the tumor vasculature is often described as dilated [30, 34]. Since the average diameters at the DMBA treated cheek pouches were always higher than the average diameters at the control cheeks, the limited sample size might be a reason for our failure to observe statistically significant differences. Experiments with larger sample size might help to investigate the dilation which was not observed in this study.

The performance of the Gabor filter is affected by vascular contrast as demonstrated in Fig. 4 and Fig. 6. Vascular contrast could potentially decrease with hyperkeratinization and hyperplasia. Contrast in the DMBA treated cheek pouches decreased from 0.24 to 0.14 (Table 3). With lower contrast, the Gabor algorithm will identify vasculature with worse sensitivity compared to manually traced gold-standard masks. Therefore, it is important to increase vascular contrast to improve the performance of the Gabor algorithm. Agents such as paraffin oil maybe used to reduce tissue scattering in clinical settings [35, 36], which in turn could improve the signal to background ratio. Although the discrepancies between the manually traced mask and the Gabor mask increases when the contrast decreases, the Gabor algorithm can still identify vasculature objectively and rapidly. The time to generate a single manually

Biomedical Optics EXPRESS

trace mask is approximately 2 hours for each image whereas the time to generate a Gabor mask is only about 40 seconds.

Although our results demonstrated statistical significance using non-parametric analyses, we are aware that our results could suffer from sampling errors and type 2 errors as our sample size for the SCC group is only 11. In addition, images were obtained only at 1 randomly determined location each time a cheek pouch was imaged. Vascular features might be different at different locations in the same cheek pouch. Increasing the sample size and collecting vascular images from different locations in the same cheek pouch can account for the heterogeneous vascular features in the hamster cheek pouches during cancer development.

The described CPDF-microscopy in this study is a label-free technique, thus minimal preparation is needed prior to imaging the vasculature. With the help of Gabor filter based algorithm, the vascular features can be quantified automatically and rapidly once the images are captured. These advantages will reduce the required training and make our approach simple-to-use. In the current CPDF-microscopy, the most expensive device in the system is the LED light source module which costs around $2000. However, the cost of our system can be further reduced by using a less powerful LED system in the future design. In the current design, CP is responsible for a substantial amount of optical power loss. A major reason that CP was used in our system is that it can easily eliminate the backscattered light from the uneven surface of the cheek pouch. However, the backscattered light from the uneven surface can potentially be removed by placing an optical flat (such as a coverslip) on top of the sample [35]. Removing the polarizer and analyzer will result in a four-fold increase in power. By increasing the optical throughput, a weaker, and therefore less expensive, LED can be used.

Future studies include incorporating optical filters for spectral imaging to estimate tumor hypoxia, a crucial cause for tumor angiogenesis [37], during the carcinogenesis. Measuring tumor hypoxia has shown promise for cancer detection [38–40]. Therefore, the addition of physiological endpoints to the currently available vascular features could potentially enhance the contrast between malignant and normal tissues. In addition to the contrast enhancement, a portable design will be considered for our next generation vascular imaging system since our goal is to detect epithelial cancers such as head and neck cancer in LIMCs. Studies have shown the feasibility of using a portable DF microscope to image vasculature *in vivo* [35, 41]. Moreover, since the Gabor filter failed to characterize small features in the vascular images (Fig. 4(a) and Fig. 5), we excluded small vessels in this study. A future direction will be to include a higher-magnification objective lens thus assigning more pixels to the smaller vessels in order to improve the accuracy when extracting features of the small vessels.

5. Conclusion

We developed a low-cost CPDF-microscopy system with millimeter scale FOV and micron level resolution for *in vivo* vascular imaging. A Gabor algorithm and image processing techniques were used to analyze images of the hamster cheek pouch to quantify several important vascular features objectively and automatically. We observed significant changes in tortuosity and length between control and DMBA-treated cheek pouches that undergo carcinogenesis. Our preclinical study demonstrates that using CPDF-microscopy to capture vascular features is a promising approach for early head and neck cancer detection in LMICs.

Acknowledgments

The authors would like to thank the funding sources 1R01EB01157 and W81XWH-09-1-0410. The authors would also like to thank Dr. Sina Farsiu for providing the software packages and Heather Liu for hand-tracing the vessel masks.